Experimental and Numerical Analysis of 3D Printed Cement Mortar Specimens Using Inkjet 3DP

Abstract

Investigations involving the experimental and numerical analysis of inkjet (powder-based) 3DP are relatively limited for cement mortar materials. This study, by using cement mortar specimens, aimed to determine the optimum strength of 3D printed structural members in all three planes by identifying the compressive strength of cubes, the modulus of elasticity and Poisson's ratio. In addition, this study aimed to analyse and verify the numerical model for 3D printed cementitious mortar (CP) prisms and beams using an inkjet 3D printer by considering the mechanical behaviour of the printed prisms under compression. Robust and optimal mechanical properties of the 3D printed cementitious mortar obtained from laboratory testing were utilised in the simulation of structural components using ABAQUS software. As inputs for simulation, the strength properties of the printed objects in all three cartesian planes were obtained from test results. The obtained results showed that the printed cementitious materials have orthotropic properties and that the results of experiments were consistent with the analytical solutions and hypothesised model for the different geometric shapes. This finding is extremely valuable in determining the optimum features of 3D printed structures.

Graphical Abstract

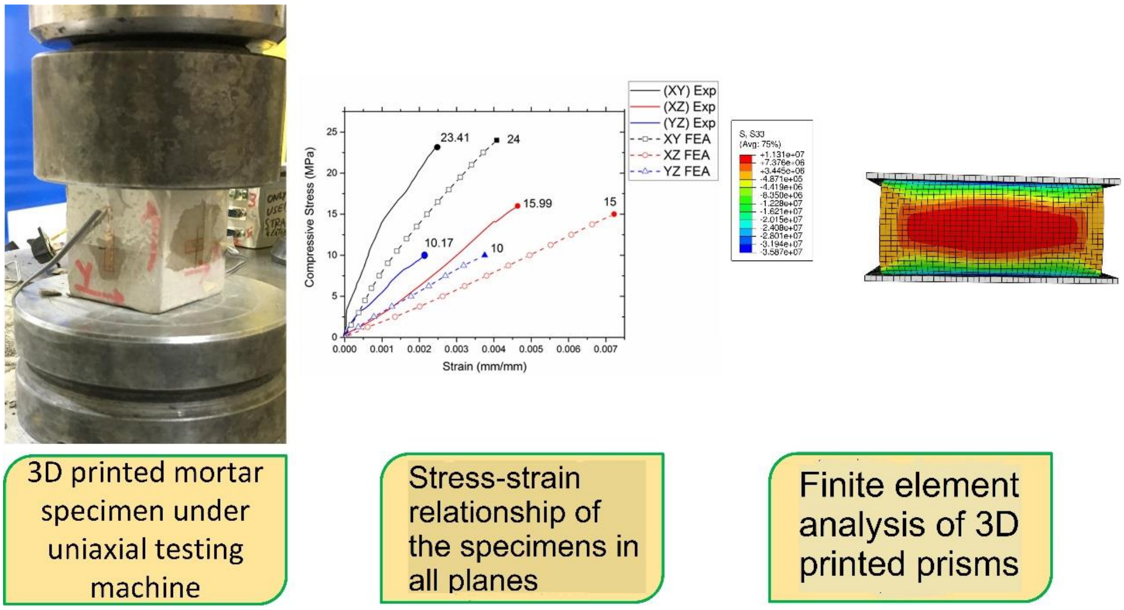

Keywords: Inkjet 3DP; printed cement mortar; orthotropic properties; compressive strength; simulation model.

Highlights

- Identified the orthotropic properties of the printed specimens perpendicular to the three planes XY, XZ and YZ.
- Obtained orthotropic compressive stress-strain diagrams of the 3D printed cement mortar specimens.
- Used a finite element analysis of the 3D printed mortar prism model and compared it with conventional results.
- Used a finite element analysis to check the deformation of cantilever and simply supported beams.

1. Introduction

According to the American Society for Testing and Materials (ASTM52900 - 15), additive manufacturing (AM) is described as a layer-by-layer printing procedure, in which a command is received from the data files of the computer-aided design (CAD) model [1]. AM consists of seven techniques [2], as shown in Table 1.

Table 1. The seven techniques of AM are best-known in various fields [2]

Techniques	Activator	Feeder and bed supply
Inkjet (powder-based or binder jetting)	Liquid binder	Powder[3],liquid binder
Directed energy deposition	Laser, electron beam or plasma beam	Wire or powder
Material extrusion	Heat, ultrasound or chemical reaction	Slurry [4]or wire
Material jetting (Polyjet)	Radiation source or a temperature field	Liquid resin or wax
Powder bed fusion	Thermal energy (laser, electron beam, infrared light)	Powder
Sheet lamination	Thermal, chemical reaction or ultrasonic transducer	Sheet
Stereolithography	Ultraviolet light	Photosensitive resin

AM can be used to create objects of complicated shapes without the help of formwork, with these techniques being applicable mostly to small structural components [5]. These techniques are cost-effective, time-saving and do not require machining [6]. AM has grown rapidly due to its advantages in various industries and is currently being used in various fields such as medicine, the automotive, aerospace, food and construction industries, and in architecture [7]. Generally, the 3D modelling and printing process follows the procedure described below [8]:

a) Using CAD software to draw a 3D model.
b) Transforming the model into a standard triangulation language (STL) format.
c) Slicing the STL file into thin layers.
d) Conveying the geometric information in every layer to the 3D printer in sequence.
e) Constructing one layer over another, according to the received data from the CAD software.

Over recent decades, inkjet 3DP techniques have been rapidly developed for many applications. This has occurred not only in the development of the techniques but also in the size of the printers [9]. Dini [10] developed a large 3D printer, called D-shape, which created complicated geometries with sand and magnesium-based binder. This invention was applied to create 3D printed structures in mortar and concrete utilizing inkjet printers. This technique is very promising and reliable mechanical strength results can be achieved. A similar technique is also used in the 3DSystem inkjet printer named ProJet (360). This technique can be used to create various structures and geometries (see **Figure (1)**).

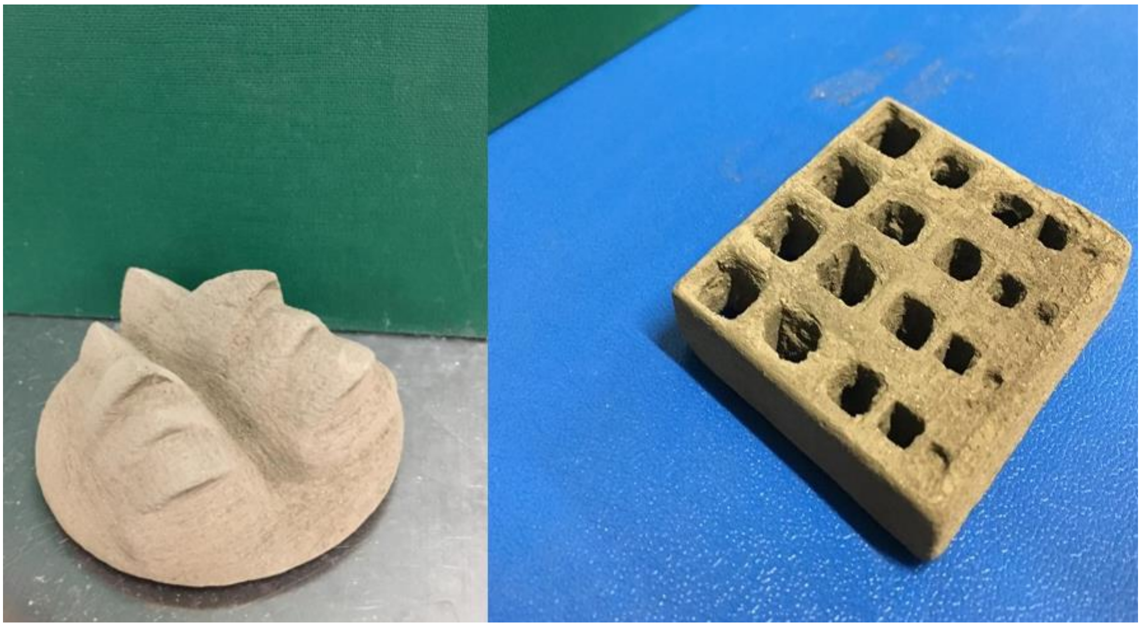

Figure (1): different geometries made of cement mortar using the inkjet 3DP technique

Only limited research on the simulation and analysis of printed objects has been conducted and research into the modulus of elasticity of 3D printed cement mortar structures, in particular, is rare. Some work was conducted on structures using calcium sulphate hemihydrate (CSH) by [11]. They found that 3D printed CSH materials have different microscopic structures from conventional CSH materials, the compressive strengths also varied. Therefore, the stress-strain relationship and compressive strength properties of 3D printed mortar specimens are the main focus of this study.

There are only a few studies on the numerical investigation of 3D printed cementitious materials due to the novelty of 3DP applications in the construction industry [12]. Development and research in this field are in the initial stages and further research is required to fully understand the details of the printed structures using different 3DP techniques [13]. Lee et al. [14] have studied different types of 3D printers such as a fused deposition modelling printer, an inkjet 3D printer and a nano composite deposition system. They found anisotropic behaviours in compressive strength in the three types of 3D printers. Khoshnevis et al. [15] proposed that, in 3D printing extrusion, the correlation of angular velocity, extrusion rate and pressure of pumping are crucial and should be considered in finite element analysis. Lowke et al. [16] stated that the inkjet printing application could be beneficial in the printing of construction components in three major ways: (1) direct printing of construction members; (2) printing formwork, filling it with conventional concrete and then removing the formwork; (3) similar to point (2) but the formwork remains as a permanent part. These procedures may be feasible to use in the inkjet printing process but the particle size in the matrix could present a challenge. However, the point which was controversial in the study of [16] was the situation where the printer could perform these procedures while being converted to a composite 3D printer. In another words, combining the inkjet 3D printer and fused deposition modelling into one printing process.

The earlier studies of [17] proposed reinforcement for the extrusion printing process, but there was not any reinforcement propose for the inkjet 3D printing. The limited use of inkjet 3D printing may be a major reason that most of the research focus has been on extrusion applications rather than inkjet 3D printing.

Results of experimental and numerical simulation of 3D printed specimens using cement mortar as the base material are presented in this paper. Earlier studies found that the 3D printed specimens had a layered orthotropic microstructure, with each layer comprised of parallel strips [18]. However, in this study, a compression test was conducted to determine the ultimate compressive strength and the experimental results, a stress-strain relationship, was obtained to determine the modulus of elasticity and Poisson's ratio of the 3D printed objects. The Poisson's ratio was found using lateral strain on both sides of the 3D printed specimen. These results were used as input parameters in the simulation model to verify the experimental results and to illustrate the orthotropic behaviour of 3D printed specimens.

2. Experimental and Numerical Preparation

2.1 Materials and Physical Properties

The preparation of the materials was described in a previous study by the authors [19]. A gypsum plaster material (CSH) was replaced with cement mortar to create 3D printed specimens. The cement mortar was a mix of Calcium Aluminate Cement (CAC) 65.3%, Ordinary Portland Cement (OPC) 29.7%, with 5% fine sand added, as indicated in Table 2. The chemical constituents of the CAC, OPC and fine sand were as follows:

Table 2. The main chemical compositions of cement mortar

Chemical Composition	Ordinary Portland Cement	Calcium Aluminate Cement	Fine Sand
Silica (SiO_2)	17 ~ 25%	≤6.0	~100%
Lime (CaO)	60 ~ 67%	≤39.8	-
Alumina (Al_2O_3)	3 ~ 8%	>37.0	-
Iron oxide (Fe_2O_3)	0.5 ~ 6%	≤18.5	-
Magnesia (MgO)	0.1 ~ 4%	~1	-
Mix Proportion	65.3%	29.7%	5%

2.2 Specimen Preparation by 3D Printer

In the present study, inkjet printing was used to produce specimens, with the actual printing procedure detailed in **Figure (2)**. The roller on the back of the printer transfers the powders from the back of the printer. The printing process begins once the water droplet is discharged from the head of the printer. On the completion of the printing process, the printed objects are dried in the chamber for 2 hours. Finally, the build chamber is vacuumed and the printed parts are properly brushed.

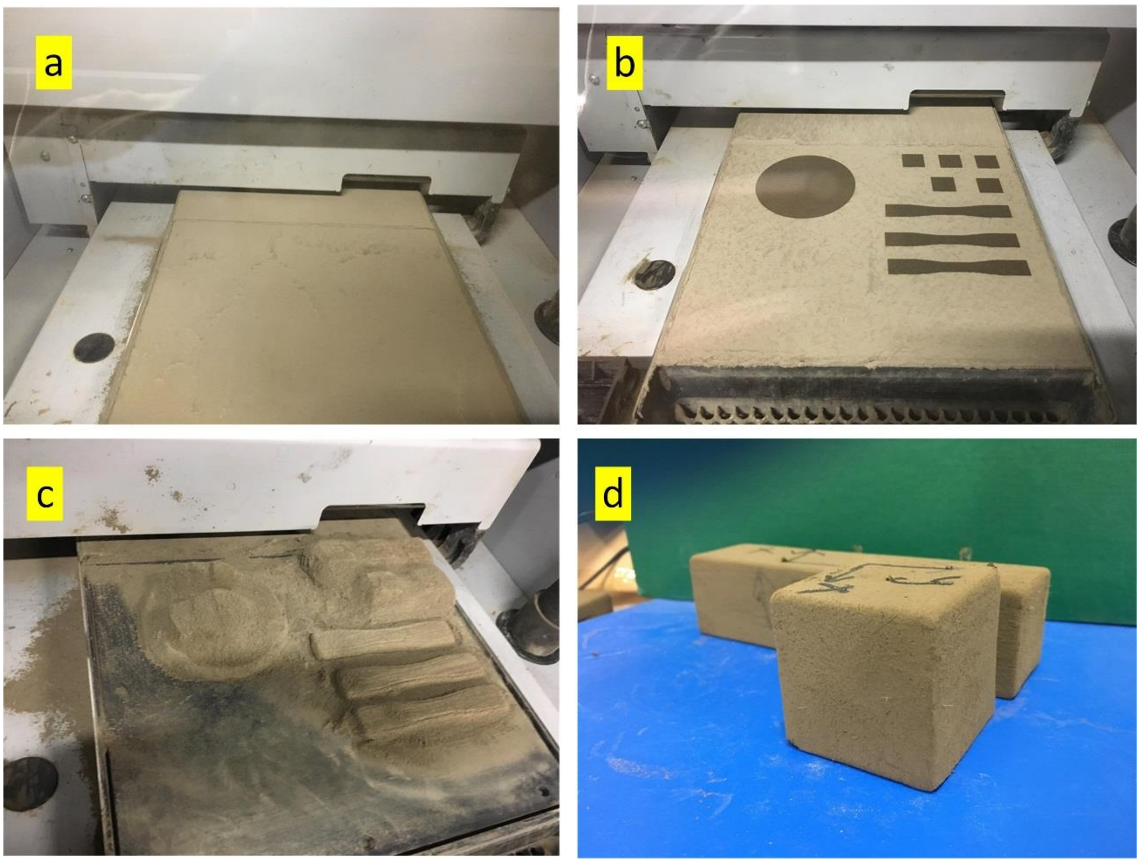

Figure (2). Printing procedures of 3D printed cement mortar specimens: (a) layering powder on build-chamber, (b) printing process, (c) removal of printed part and cleaning, (d) green part of the printed specimen

2.3 Printed Specimen Properties

The surface of printed cubic mortar specimens of 50 mm size were examined using a scanning electron microscope (SEM) and a high-resolution digital camera. **Figure (3)** shows the microstructural surface of the 3D printed specimen as follows:

1. Layered surface: The 3D printed mortar specimen has an obvious microstructural layer of 0.1 mm. As shown in Figure (3a), the layers can be seen clearly in the XZ plane.

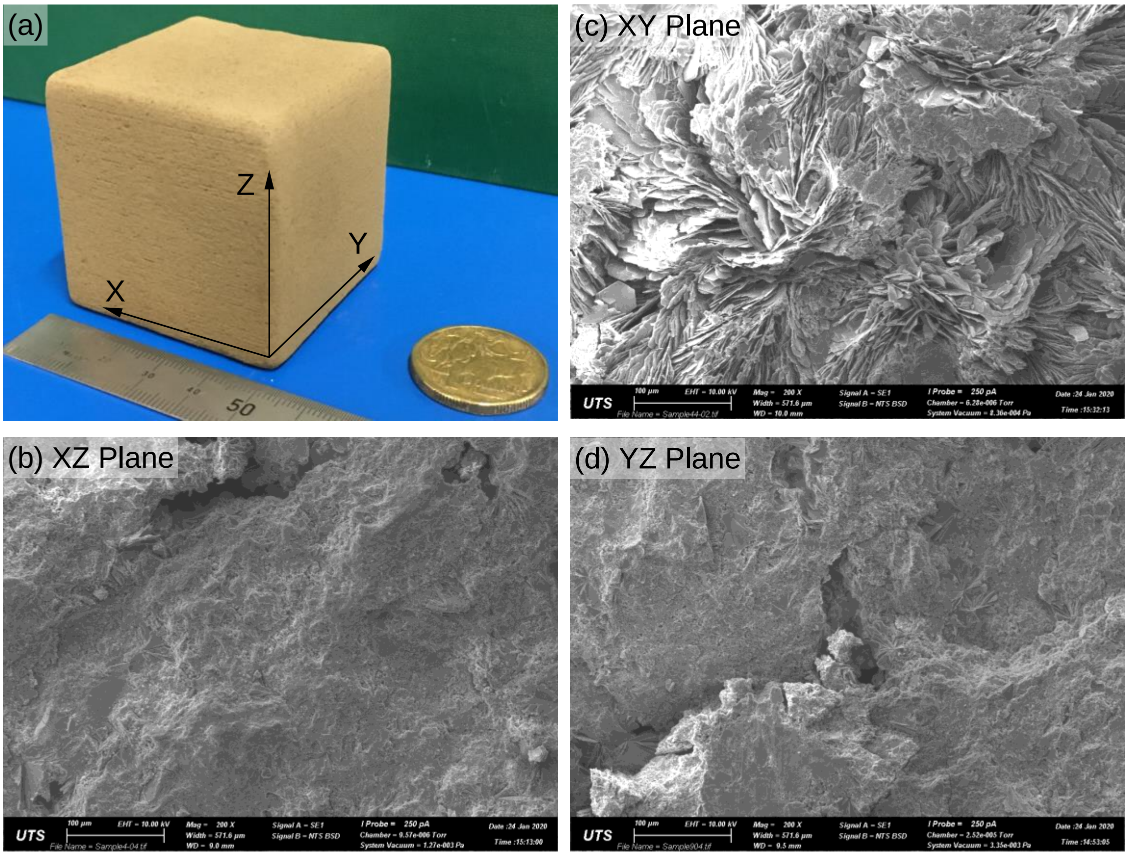

Figure (3). (a) Typical printed specimen and scanning electron microscope analysis of the printed specimen in three planes (200 ×), (b) XZ plane, (c) XY plane and (d) YZ plane

For further clarification, **Figure (4)** shows the layer thickness on the surface of the printed specimen. The thickness of the layer determined by using Fiji software after setting the scale in the Menu bar. In the Analyze bar used measure to measure the thickness of the layer and the same procedure also used to measure crack on the same specimen. The crack appeared to occur between layers.

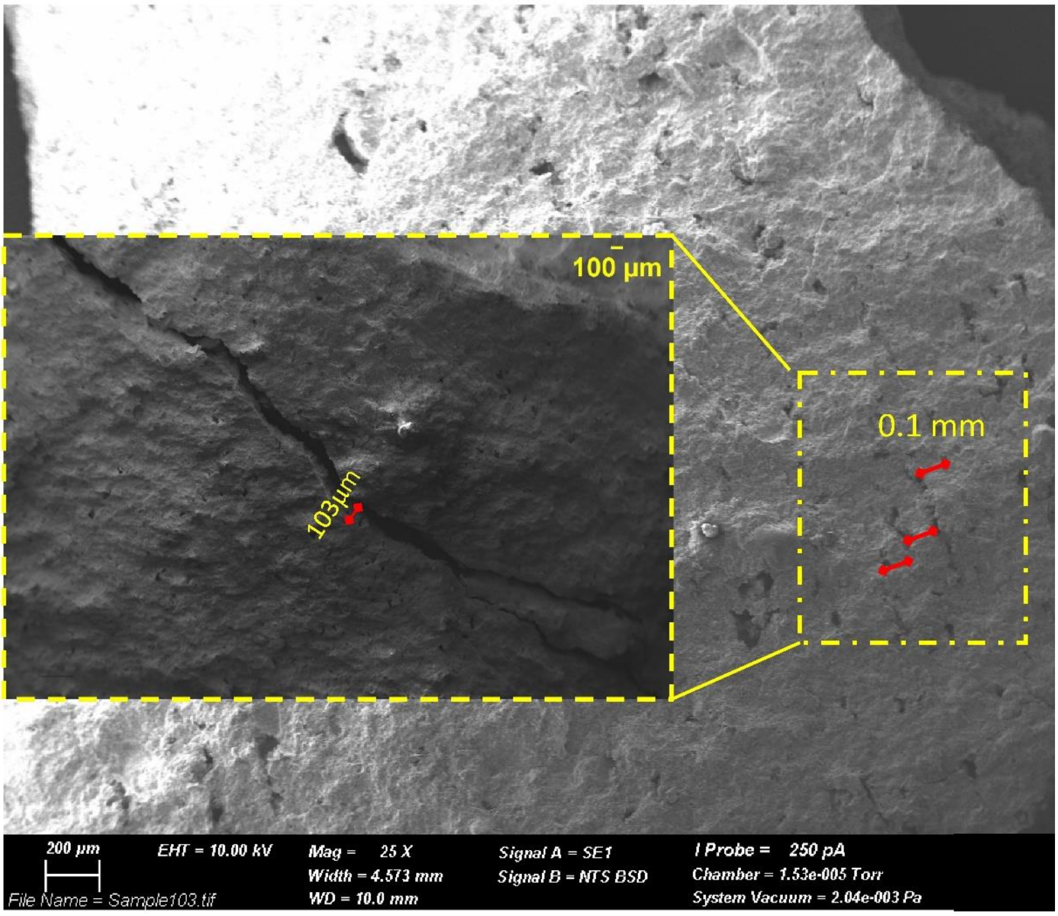

Figure (4). SEM of printed specimen with indicate the thickness of layer 0.1mm and the crack pattern between layers

2. Striped lines in each layer: There are many stripes in each of the printed layers, with the stripes occurring in the XY plane. The printhead moves on the surface of the powder which is in the XY plane. The size of the stripes is dependent upon the size of the printhead (see **Figure (5)** for details of the printhead).

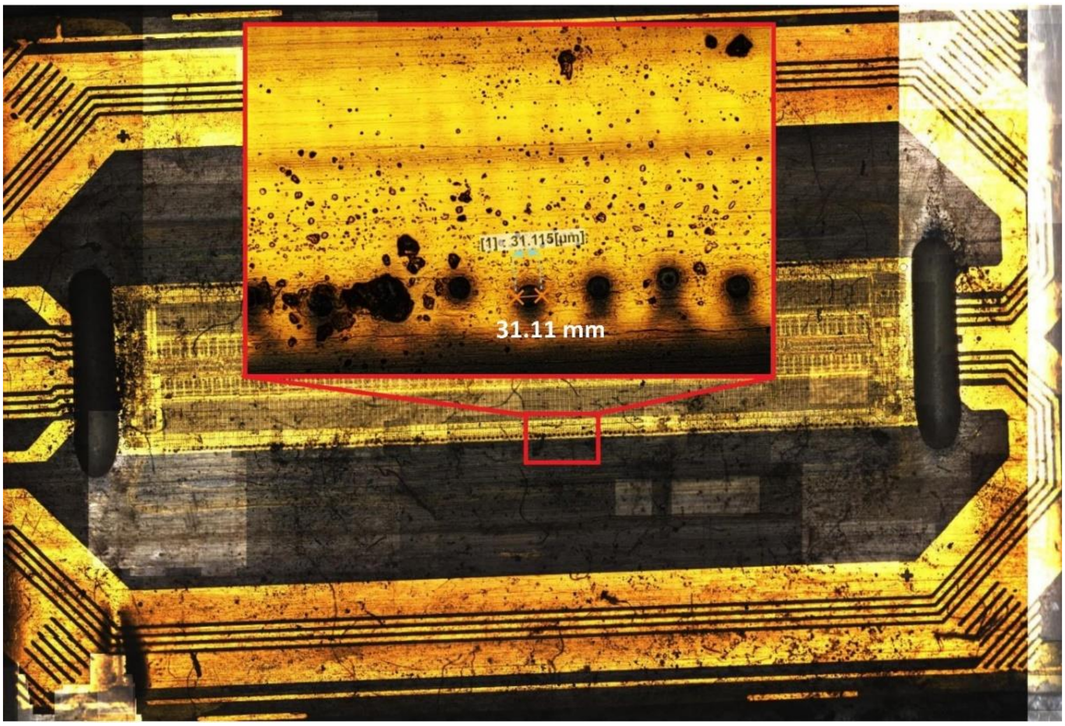

Figure (5). Laser scanning captures HP 11 printhead orifices; the total number of orifices is 304

3. Orthotropic properties: Generally, the XZ plane has the roughest surface compared with the other planes. The YZ plane is the smoothest plane (12.9±1.8μm) and the roughness level (Ra) of the XY plane (26.7±9.2μm) falls between those of the XZ (40.4±17.9μm) and YZ (12.9±1.8μm) planes. **Figure (6)** shows a laser scanning surface roughness profiles of XY, XZ, YZ planes for the printed surface.

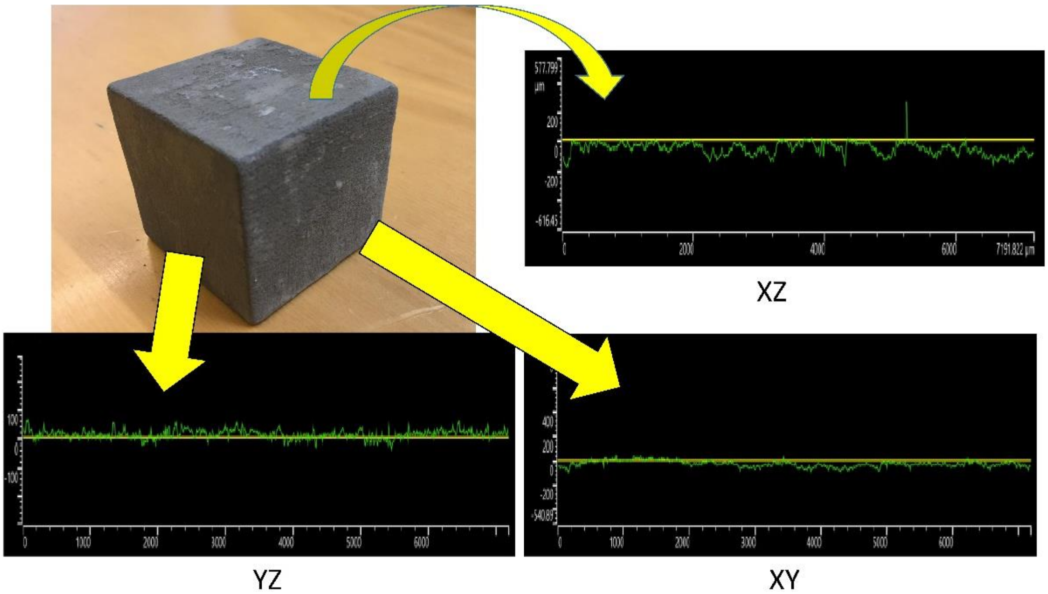

Figure (6). Laser scanning of surface roughness profiles for XY, XZ and YZ planes

2.4 Binder Solution (water) and Printhead Specification

The binder solution ZB 63 was used as an activator to bind powder particles on the build-chamber. The main components of the binder solutions ZB 63 are humectant (polyvinyl alcohol or glycerol) and water, as indicated in **Table 3**.

Table 3. Specifications and chemical composition of the binder solution ZB 63

Specification	**Value**
pH (20°C)	9.8
Melting point/range (°C)	0
Boiling point/range (°C)	100
Density (g/cm^3)	1
Surface tension (N/cm)	0.00045
Viscosity (g/cm-s)	0.0135
Chemical composition of binder %	
Water	95%
2-pyrrolidone	~5%

The printhead of the 3D printer is an HP 11 (C4811A) with 304 nozzles (see Table 4).

Table 4. Technical details and specifications of the printhead

Printhead technology	HP Thermal Inkjet
Printer Resolution	300 × 450 DPI
Inkdrop	18 pl
Printhead orifices (nozzles)	304
Nozzle diameter	~31 µm
Area of the orifices on the printhead	15× 5 mm
Dimensions of printhead	109.98 × 25.91 × 148.08 mm

2.4 Mechanical tests

The axial compressive strength, elastic modulus and Poisson's ratio were systematically determined for the 3D printed specimens in all three planes, as shown in **Figure (7).** Crack patterns and failure features of the printed specimens are also shown in **Figure (8)**.

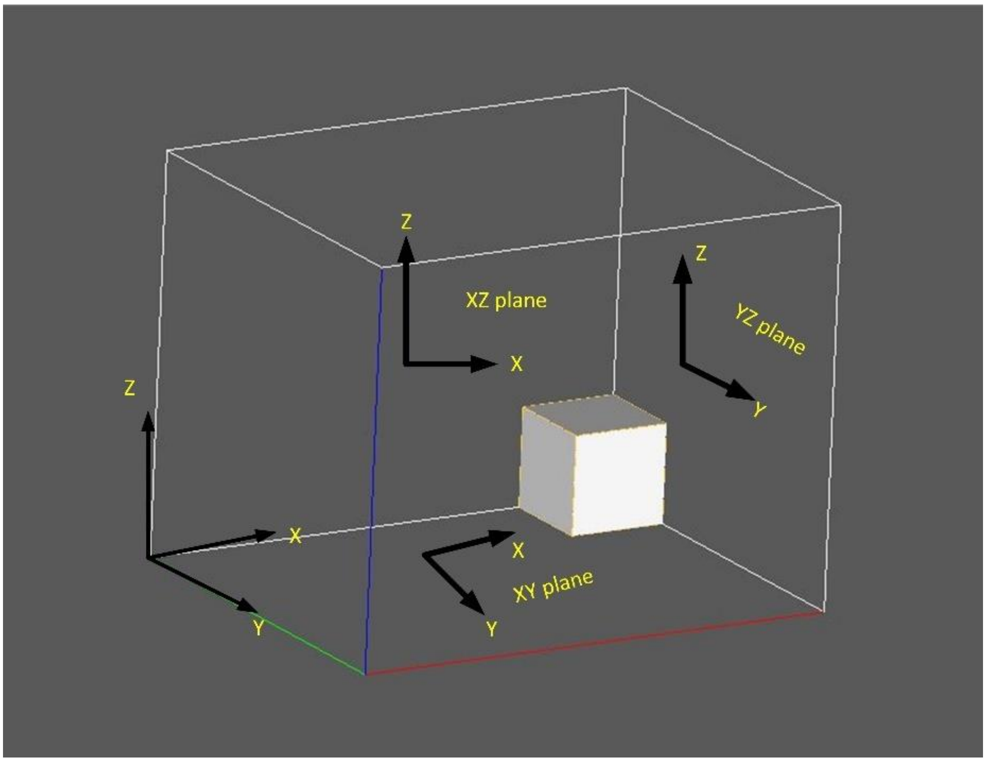

Figure (7). Different planes of the printed specimens

Table 5 shows three sets of printed cubes which were examined perpendicular to all three planes (XY, XZ, YZ). Three specimens of each set were tested for compressive strength. These sets were made from the same ingredients with a layer thickness of 0.1 mm.

Table 5: Size and number of specimens

Specimen label	**Plane**	**Number of Specimen**	Specimen Size
S 1.1		3	
S 1.2	XY	3	
S 1.3		3	
S 2.1		3	
S 2.2	XZ	3	50×50×50 mm
S 2.3		3	
S 3.1		3	
S 3.2	YZ	3	
S 3.3		3	

The specimens labelled S 1.1 to S 1.3 were loaded in the Z-direction while the other samples, labelled as S 2.1 to S 2.3 and S 3.1 to S 3.3, were loaded in the Y-direction and X-direction, respectively. Strain gauges were attached at the middle of the horizontal and vertical dimensions of the specimens. Only the vertical direction (axial) was selected for the strain measurement. The grid length of gauges was 30 mm and the electrical resistance was 120 Ω. All specimens were tested after 28-days of curing. The postprocessing of the printed part was: 3 hours in the furnace, 28 days in water and then in the furnace again for 3 hours (the sequence of curing in the 3D printing technique).

A typical configuration of the strain gauge attached to the surface of the specimen in the axial and lateral directions is shown in **Figure (8)**. The strain of specimens at the initial stage of the loading on the 3DP mortar specimens was minimal. In the initial phase of loading, the stress-strain response was unstable and this has been confirmed by other researchers [20]. This instability of strain response at the commencement of the applied load on the specimens could be due to the interlayer gap which causes movement and friction between layers.

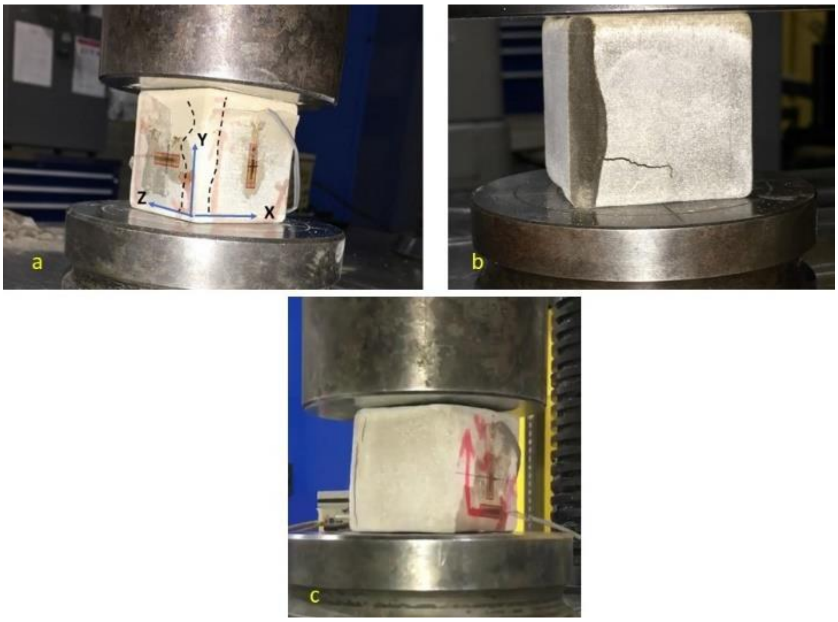

Figure (8). (a) Strain gauge and failure description on a 50×50×50 mm specimen (black dashed lines represents the crack propagation path), (b) Cracks on the XZ plane, (c) Cracks on YZ plane

The cracks started when the specimens reached the peak load. The cracks formed and propagated along the direction of loading close to the edge of the specimens in both the (XZ) and (YZ) planes. The direction of layers for the printed specimens had a major influence on the cracking propagation path. Both planes, namely, (XZ) and (YZ) had printed layers in the direction of loading, and this is the main factor that caused cracking in the vertical direction. Therefore, it is evident that the cracks initiated and took place between layers which extended to the exterior of the specimens. The red and yellow dashed lines in **Figure (9)** indicate the crack lines on the surface of the (XZ) and (YZ) specimens.

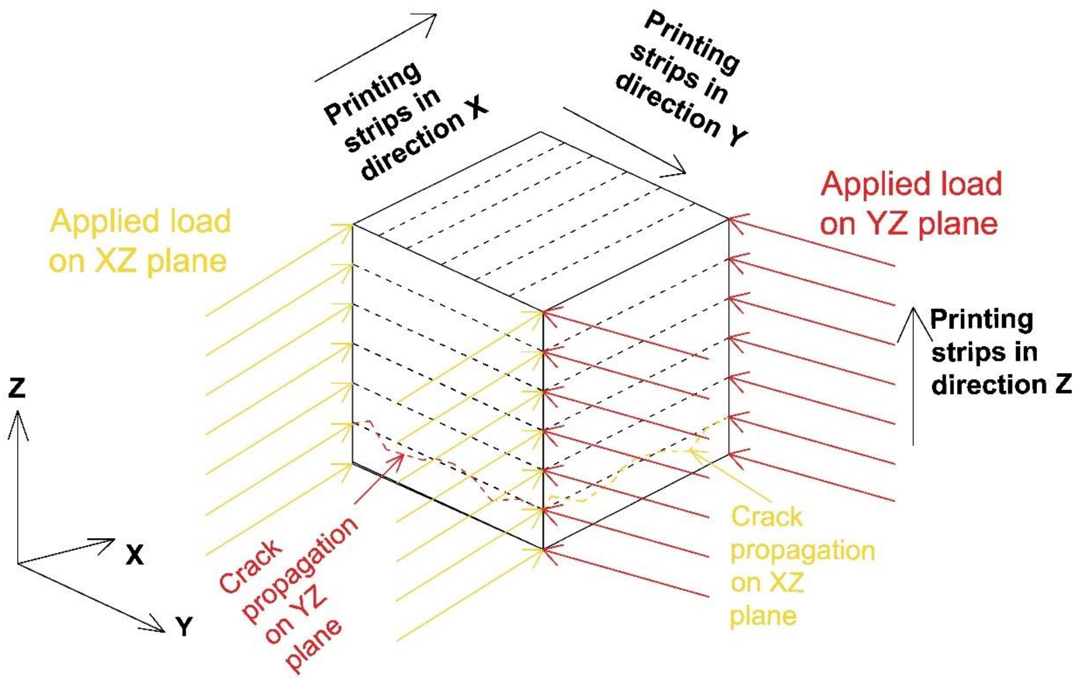

Figure (9). The crack path on the 50×50×50 mm XZ and YZ specimen (red and yellow dashed lines represents the crack path)

The crack propagation mechanism on the specimen's surface delaminated the printed layer of mortar from another layer. It is obvious that cement mortar and concrete materials are brittle materials [21], therefore, the specimen could not withstand the excess load and started to detach at the weakest bond of the specimen. In a 3D printed part, the layers constitute a weakness in the specimen. However, the edge of the specimen is not supported by other layers, so it is weaker than the rest of the 3D printed specimen.

A gantry holds the printhead, with both being held by a rail and both being able to move along the X and Y axes [22]. The printed part could be improved by using a double axis gantry, with each perpendicular to the other, to print layers across each other. This solution would result in a tougher printed part that is more durable and the crack propagation path then changes to diagonal or stair shaped cracks.

3. Results and Discussion

3.1 Experimental Program

3.1.1 Compressive Stress-strain Diagram

A compressive stress-strain diagram is used to determine the resistance of the printed cement mortar materials to the applied load which is applied externally to the specimen.

Figure (10) shows the stress-strain relationship of the 50×50×50 mm specimens for all three planes of cement mortar specimens. In the inkjet 3DP specimens, the results are different from conventionally casted mortar/concrete. The casted concrete/mortar has a uniform result for all planes and directions. Further, increasing the size of 3DP specimens causes an increase in compressive strength. However, increasing the size in the conventionally casted specimens causes a reduction in the compressive strength results [23].

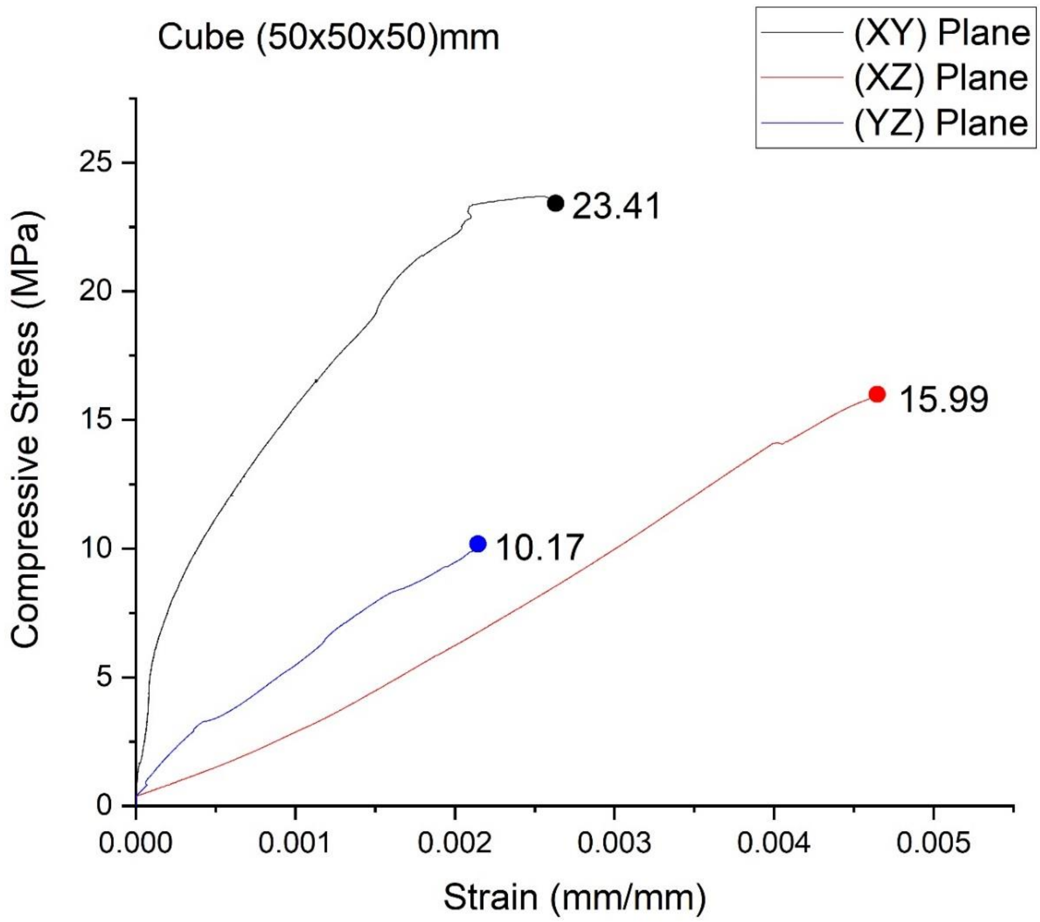

Figure (10). Maximum value of compressive stress-strain diagram of the printed cube 50×50×50 mm for all three planes in the cement mortar specimen

According to ACI318-14 [24], the modulus of elasticity of concrete can be determined by the following equation (1). The same equation could also be used for printed specimens.

$$E_c = 4700\sqrt{f'_c} \qquad (1)$$

where f'_c is the specified compressive strength of concrete in MPa, E_c is the modulus of elasticity of concrete in MPa.

Finite Element Analysis (FEA) is conducted to verify the mechanical characterisation of the 3D printed specimens. The stress-strain results of the 50×50×50 mm 3DP specimens are presented in **Figure (10)**. The printed specimens were prepared to measure E_c and v according to ASTM:C109/C109M [25]), with strain gauges attached to the surface of the specimens to measure the axial strains and lateral strains, respectively. The elastic modulus and Poisson's ratio of the materials were obtained from the results (see **Table 6** and **Table 7**).

Table 6. Compressive strength and Elastic modulus of 3D printed cement mortar specimens

Specimen label (50×50×50)mm	Compressive Strength (MPa)		Elastic Modulus (GPa)		Plane
	Value	Average	Value	Average	
S 1.1	23.04	23.21	9.50	9.57	XY
S 1.2	23.41		9.65		
S 1.3	23.20		9.57		
S 2.1	15.99	15.95	3.44	3.55	XZ
S 2.2	15.97		3.65		
S 2.3	15.91		3.55		
S 3.1	10.17	10.15	4.75	4.63	YZ
S 3.2	10.13		4.64		
S 3.3	10.15		4.51		

Table 7. Poisson's ratio of 3D printed cement mortar specimens

Specimen label (50×50×50)mm	Poisson's Ratio			
	v **YZ**	**Average**	*v* **XZ**	**Average**
S 1.1	0.31	0.29	0.31	0.32
S 1.2	0.27		0.29	
S 1.3	0.29		0.35	
	v **YZ**		*v* **YX**	
S 2.1	0.24	0.26	0.31	0.31
S 2.2	0.27		0.31	
S 2.3	0.27		0.30	
	v **ZX**		*v* **XY**	
S 3.1	0.19	0.15	0.14	0.16
S 3.2	0.14		0.14	
S 3.3	0.13		0.19	

Figure (11) shows the stress distribution on the plane of the 3D printed cube.

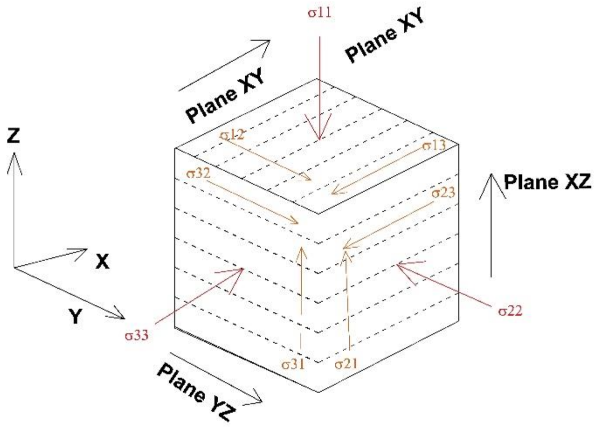

Figure (11). Stress distribution diagram on the three planes of the 3D printed cube

The results of the cement mortar materials were entered into ABAQUS software. Based on equations 2 to 11, it was found that the cubes had orthotropic characteristics in all three directions (see **Table 8 and Figure 9**). The following equations define the orthotropic materials in the ABAQUS software [26]:

$$D1111 = E1(1 - v23v32)\Upsilon \quad (2)$$

$$D2222 = E2(1 - v12v31)\Upsilon \quad (3)$$

$$D3333 = E3(1 - v12v21)\Upsilon \quad (4)$$

$$D1122 = E1(v21 + v31v23)\Upsilon = E2(v12 + v32v13)\Upsilon, \quad (5)$$

$$D1133 = E1(v31 + v21v32)\Upsilon = E3(v13 + v12v23)\Upsilon, \quad (6)$$

$$D2233 = E2(v32 + v12v31)\Upsilon = E3(v23 + v21v13)\Upsilon, \quad (7)$$

$$D1212 = G12, \quad (8)$$

$$D1313 = G13, \quad (9)$$

$$D2323 = G23, \quad (10)$$

$$\Upsilon = \frac{1}{1 - v12v21 - v23v32 - v31v13 - 2v21v32v13} \quad (11)$$

where, E is Young's modulus, and v is Poisson's ratio. The shear modulus is known as G, which can be found according to the Equation, $G = E/2(1 + v)$. As an engineering constant, the D matrix defines the property of orthotropic materials. **Table 8** lists the orthotropic properties of 3DP cementitious mortar.

Table 8. Orthotropic properties of 3DP cubes cement mortar

D1111	*D2222*	*D3333*	*D1122*	*D1133*	*D2233*	*D1212*	*D1313*	*D2323*
11506.7	4284.7	5342.3	4190.18	2396.4	915.90	6108.1	2343	2916.9

3.1.2 Simulation of the structural member model

Before creating a model, it is necessary to know the 3D printed modulus of elasticity and Poisson's ratio in all three planes of the printed specimens.

To create a model in ABAQUS, a typical model with a mesh of standard hexahedron properties was chosen with an approximate global size of (0.05). Due to the limited use of cement mortar in construction, a mortar masonry block with dimensions of 390×190×190 mm and meeting Australian standard [27] was chosen (see **Figure (12)**). This model was simulated numerically using ABAQUS, with loads being applied in all three orthogonal planes (XY, XZ, YZ) as shown in **Figure (12)**.

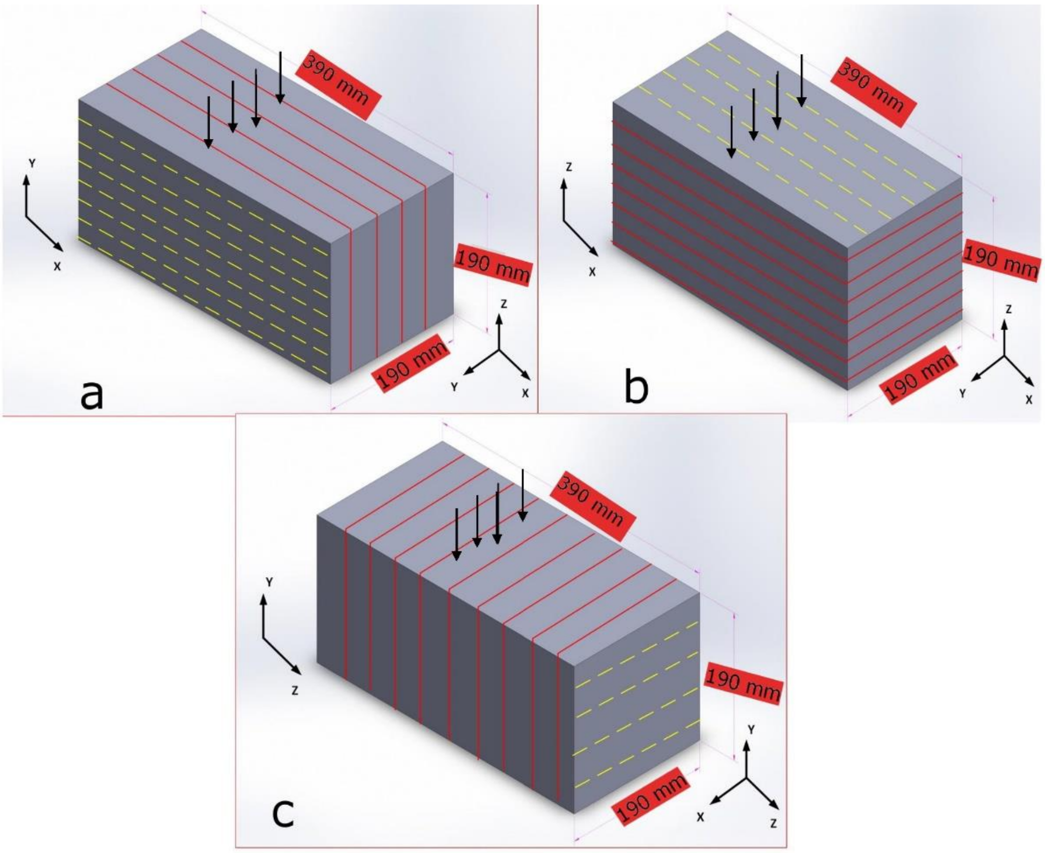

Figure (12). Load applied on the three planes of the masonry block in ABAQUS: (a) XY loading direction, (b) XZ loading direction, and (c) YZ loading direction

The load was applied in the simulation analysis as a uniform static-load for all the planes under the same load conditions. Progressive failure analysis was conducted on all specimens as shown in **Figure (10)**. The numerical simulation of prisms (masonry block) was conducted in two stages: first, using the gravity load, the initial stress in the block was simulated then, in the second stage, the vertical load was statically applied until the specimens failed. The vertical load was applied using a uniform load on the top surface of the block while the bottom surface of the block was restrained by a fixed support. The compressive loading strength test was simulated for all three planes (XY, XZ, YZ) on the masonry block with the results presented in **Figures (13) to (15)**.

Figures (13) to (15) show that the direction of printing the specimens (i.e. different directions of loading) had a significant effect on the mode of failure of the specimens, which were different for each plane for the strain and stress of the masonry block. Error! Reference source not found. shows that the maximum resistance of the structure in the (XY) plane was the highest, with an average stress of 24 MPa. In the (XZ) plane, the stress was 15 MPa. When the load was applied in the (YZ) plane, the stress was the lowest, at 10 MPa. The results show that printing in a different plane had a substantial influence on the overall stress-strain diagram of the structure. This is significant and indicates the importance of carefully selecting a suitable printing plane before fabricating the 3DP scaffold.

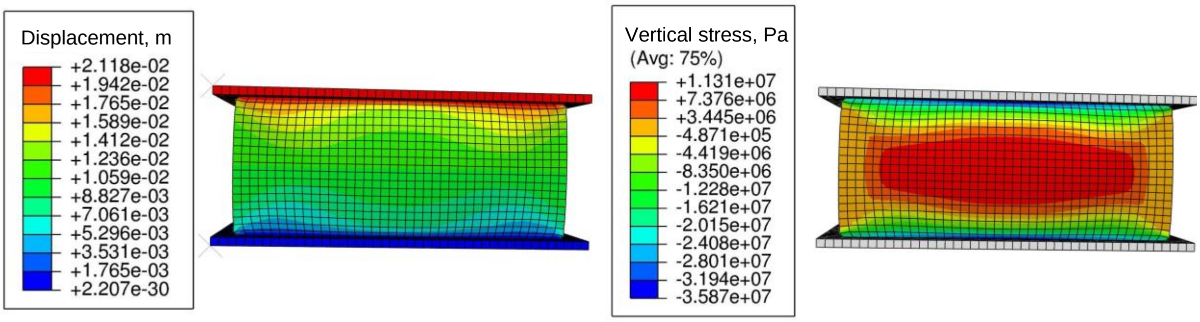

Figure (13). XY plane displacement and stress failure of the masonry block under a compression test

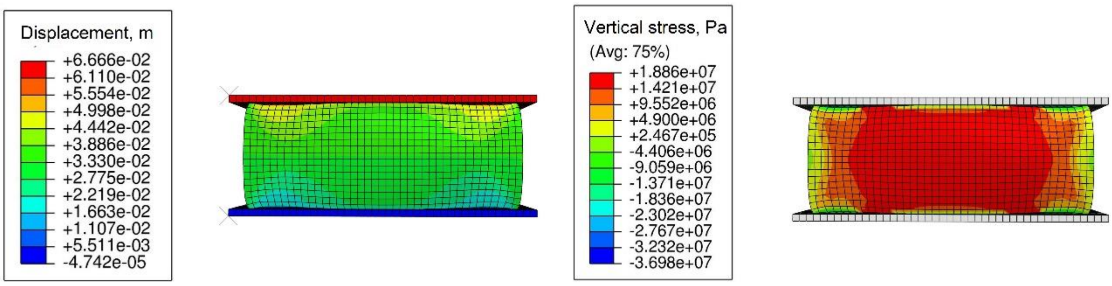

Figure (14). XZ plane displacement and stress failure of the masonry block under a compression load

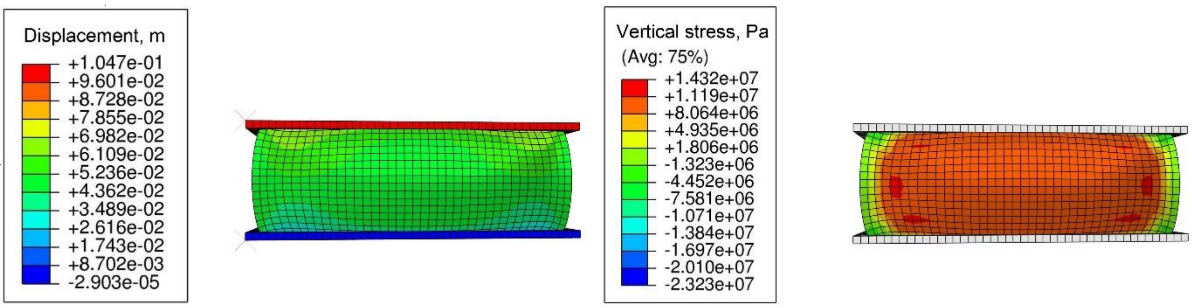

Figure (15). YZ plane displacement and stress failure of the masonry block under a compression load

The thickness of the printed layer of all specimens was 0.1 mm. A thinly printed layer might cause a layer of detachment and interlayer cracks. The detachment of these thin layers most probably occurs due to pores and gaps between the printed layers. The weakest region would certainly be between the layers. Another crucial point of concern is the delay between printing layers [28]. Another study [29] investigated how to reduce the delamination and detachment of the printed layers. However, further studies are required to prove the delamination of the printed specimens and interlayer cracks. **Figure (4)** shows the effectiveness of the layer SEM of delaminated layers and cracks in the specimens. Therefore, it is essential to fabricate structural members within the optimum printed thickness. Irrespective of the orientation of the printed specimens, different layer thicknesses have a major impact on the compressive strength of the printed part [30], confirming that medium thickness is related mostly to the particle size distribution of the materials.

The FEA results of the compression test for the three planes are shown and compared in **Figure (16)**. The loading process was applied using a static load on the masonry block. The loads applied in each plane illustrate the differences in the stress-strain diagram. **Figure (16)** shows that the specimen had the highest strength when the direction of loading was perpendicular to the layers of the printed specimen (as shown schematically in the direction of loading and layer of the printed specimen in **Figure (12b)**). Therefore, it is crucial to conduct further studies on the printed specimens at a larger scale. The results could be different from small scale printing with an earlier study finding that layer thickness had an impact on printed parts [31]. Other studies considered the effects of particle size distribution [32] and printing speed [28].

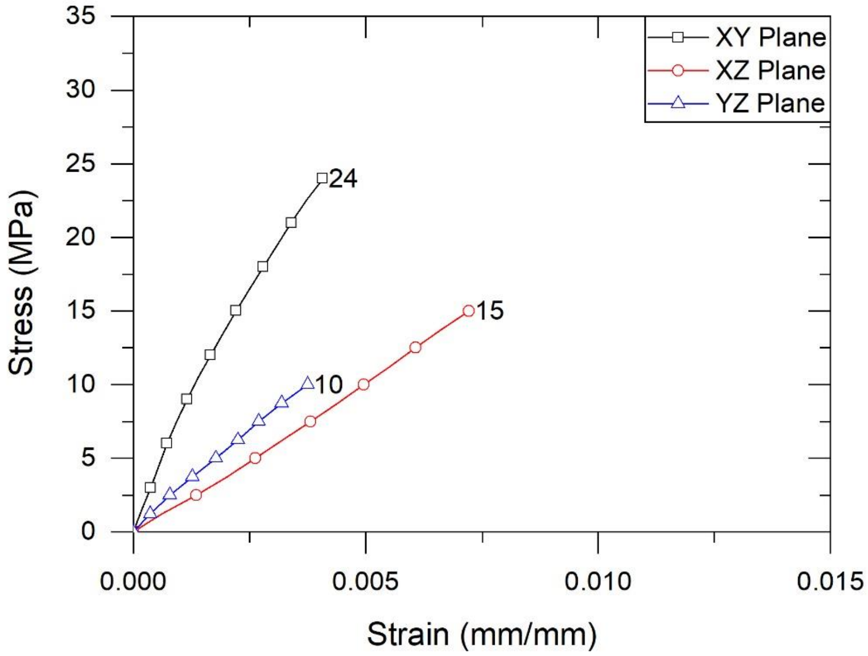

Figure (16). Stress-strain diagram for the FEA of the 3DP block under compression

4.3. Simulation for the structural member model

Both 3DP precast or 3DP cast-in-situ structural members would be suited to real-world applications. However, the printing process may change according to the printing environment. If the printing process is in a controlled environment (off-site) such as a factory or precast field, the size of the printed part will be limited due to the need for transportation and the limited dimensions of the printed frame.

Conversely, any structural members can be printed on-site as long as the robotic arm or framed gantry can extend to the required distance. Printing structural members on-site faces such challenges as potential adverse environmental conditions including high and low temperatures, rain, humidity and wind. It also challenges the segregation in the mix due to varying temperature and water content.

The FEA of a cantilever beam and a simply supported beam with dimensions of (4000×500×300) mm are two examples using a maximum stress benchmark with the constants listed (see **Tables (6) and (7)**). The FEA was performed using ABAQUS 6.13 to evaluate the effect of the printing plane in real-life structural applications. The analysed member had a length of 4m, a width of 0.3m and depth of 0.5m. It was meshed and modelled using a hexahedral structured element (approximate element size 50-100 mm for all three directional planes and both beam types) for the orthotropic properties of the structural model. Overall, the total number of elements was 4800-600, with each element size being approximately 50-100 mm. The model was analysed under a uniform distributed load for each printed member according to the maximum load, which was achieved through experimental tests. The boundary condition for the cantilever beam was constrained at the end of the structural member and the simply supported beam was pinned at one end and supported at the other end by a simple roller. The full Newton–Raphson method was used for the loading process. The printed element directions were changed in accordance with the directional print in three planes to show the differences in the displacement and maximum deflection for each of the printed structures, **Figure (17)**.

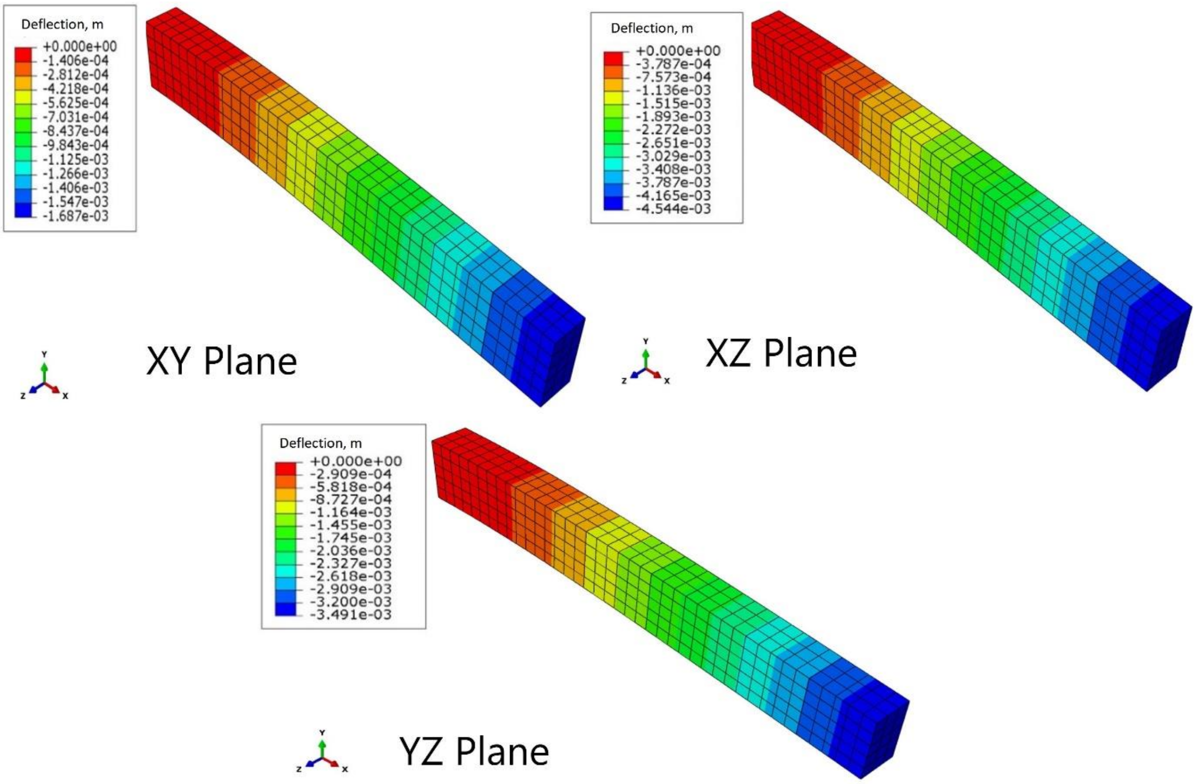

Figure (17). Cantilever beam in the XY, XZ and YZ planes

Figure (18) shows the critical locations, with most failures occurring at the fixed end of the cantilever beam and the simply supported beam. It is obvious that the maximum displacement is located at the free end of the cantilever and, in the simply supported beam, at the mid-span of the structural members, as shown in **Figures (18)** and **(19)**, respectively.

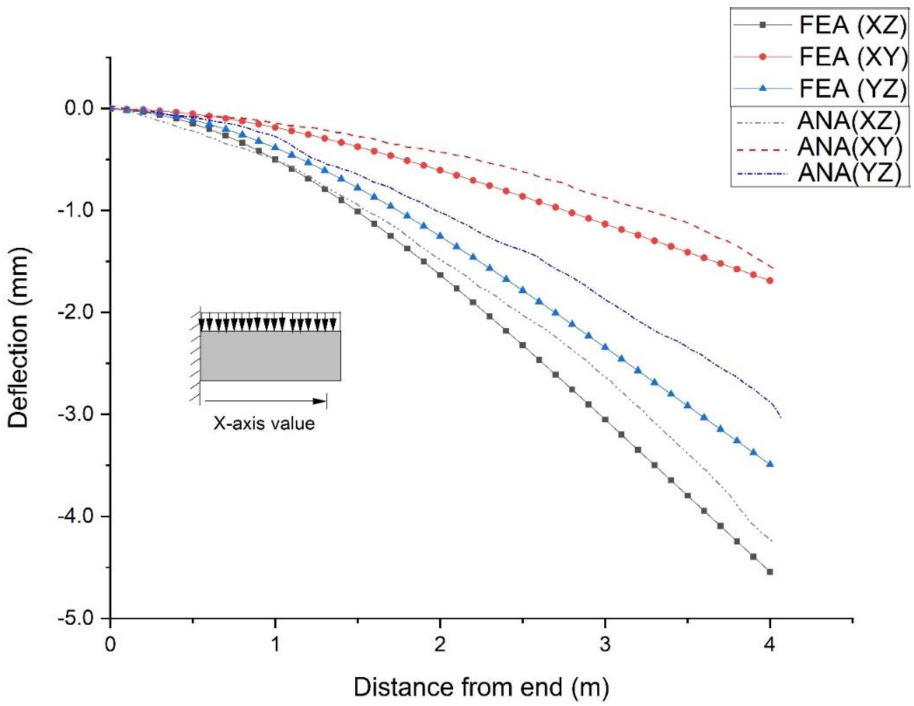

Figure (18). FEA and Analytical (ANA) results of the cantilever deflection in the XY, XZ and YZ planes

Figures (19) and **(20)** illustrates the results of deflections in the simply supported beam in all three planes (XY, XZ, YZ).

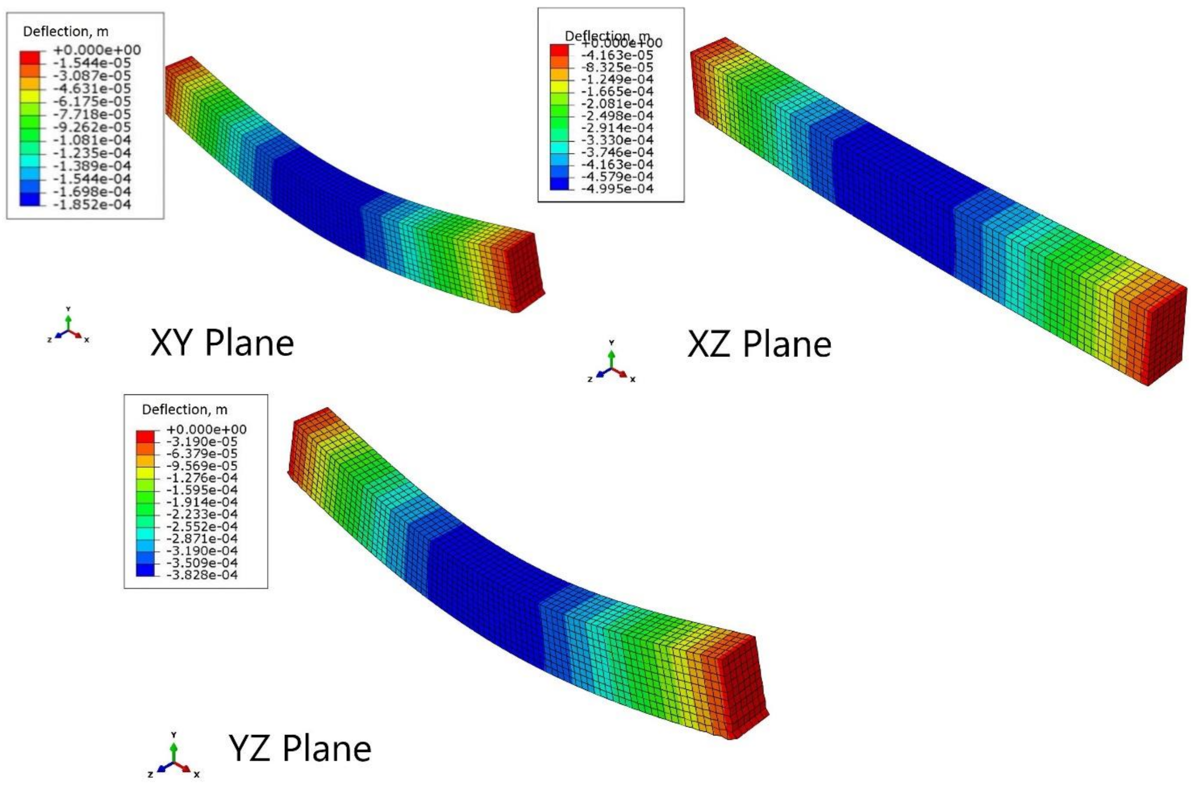

Figure (19). Simply supported beam in the XY, XZ and YZ planes

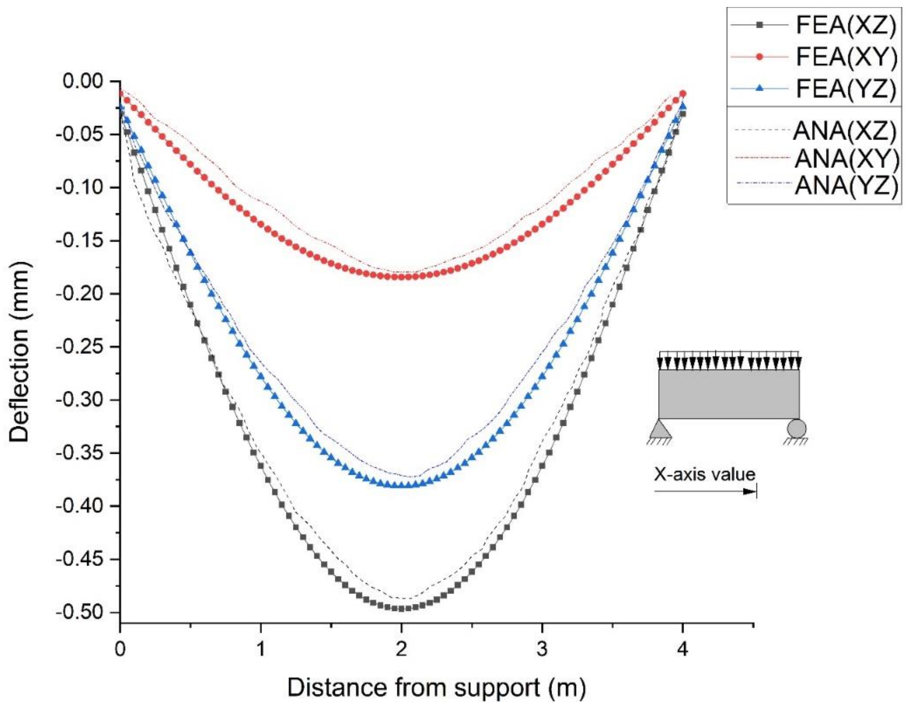

Figure (20). FEA and Analytical (ANA) results of the simply supported beam deflection in the XY, XZ and YZ planes

The maximum deflection of the cantilever and simply supported beams with a uniformly distributed load can be expressed by equations (12) and (13), respectively.

$$\delta = \frac{\omega l^4}{8EI} \quad (12)$$

$$\delta = \frac{5\omega l^4}{384EI} \quad (13)$$

where E is the modulus of elasticity of the materials, I is the moment of inertia which is the width of the structure multiplied by the depth to the power of 3 divided by 12. where ω is the uniform load on the member, l is the length of the member.

Table (9) shows the maximum deflection of the cantilever and the simply supported beam in the simulated model (FEA) compared with the analytical equations. The percentage of δ error was found to be less than 10% between FEA and an analytical method for both beams. Therefore, the ratio of error is insignificant and within an acceptable range.

Table (9) shows the maximum value of deflection for cantilever and simply supported beam in FEA and analytical calculation

Type of beam	**Max δ (FEA)***			**Max δ (Analytical)***			**%Error**		
	XY	**XZ**	**YZ**	**XY**	**XZ**	**YZ**	**XY**	**XZ**	**YZ**
Cantilever	1.68	4.54	3.49	1.61	4.3	3.3	4.3%	5.5%	5.7%
Simply support	0.18	0.49	0.38	0.17	0.45	0.35	8.2%	8.6%	9.8%
*Dimensions all in mm.									

Figures (18) and (20) show that, when loaded in the XY plane, the minimum deflections are recorded, while the XZ plane exhibited the maximum deflection for structural members. Therefore, the printing plane had a significant effect on the structural members.

To choose a suitable printing plane in the real-world of 3DP prefabrication, it is necessary to select the most durable plane when applying the load. Indeed, while the structural member printed then should be paid attention into the direction of the applied load. The most suitable loading direction is perpendicular to the layers of the printed specimen. Large scale application of inkjet 3DP, such as Dini [10] printer (well-known as a D-shape), would be most applicable to printing concrete/mortar members [33]. This technology can be developed for use in composite materials and complicated shapes for structural elements. Future studies should consider using a larger scale of the printer for structural members with thicker printed layers and larger printheads and nozzles.

4. Conclusion

This study experimentally tested 3D printed cubic specimens to identify their modulus of elasticity and Poisson's ratio. These properties were utilised in FEA modelling for structural members in different planes. The main conclusions are:

- The layered structure created a bond between the layers resulting in orthotropic properties.
- In the ABAQUS model, the experimental result of the cube (50×50×50) mm was used to obtain the modulus of elasticity and Poisson's ratio for all three planes.
- A standard block and two types of beams were studied according to their maximum compressive strength and deflection in all three planes. The results showed that the printing plane has a major influence on the compressive stress and deformation of the structure.
- The FEA deflections of the beams were verified and consistent with the results of analytical equations. The results showed that all percentages of error between FEA and analytical equations were below 10%.

Future work should focus on the potential use of concrete mixes rather than mortar mixes in inkjet 3DP technology. It is also necessary to investigate in detail the use, in this technique, of ultra-high performance concrete with advanced modification of the mix design.

Acknowledgements

The authors are grateful for the support of UTS-TechLab and UTS-ProtoSpace.

Conflict of interest

The authors declare that they have no known competing financial interests.

Ethical statements

The paper was conducted according to the ethical standards of the journal.

References

1. ISO/ASTM, Standard on Additive Manufacturing (AM) Technologies. 2015. DOI: 10.1520/ISOASTM52900-15
2. Lv, X., et al., Binder jetting of ceramics: Powders, binders, printing parameters, equipment, and post-treatment. Ceramics International, 2019. https://doi.org/10.1016/j.ceramint.2019.04.012
3. Shakor, P., et al., Dimensional accuracy, flowability, wettability, and porosity in inkjet 3DP for gypsum and cement mortar materials. Automation in Construction, 2020. 110: p. 102964. https://doi.org/10.1016/j.autcon.2019.102964
4. Shakor, P., et al., Effects of deposition velocity in the presence/absence of E6-glass fibre on extrusion-based 3D printed mortar. Additive Manufacturing, 2020. 32: p. 101069. https://doi.org/10.1016/j.addma.2020.101069
5. Upadhyay, M., T. Sivarupan, and M. El Mansori, 3D printing for rapid sand casting—A review. Journal of Manufacturing Processes, 2017. 29: p. 211-220. https://doi.org/10.1016/j.jmapro.2017.07.017
6. Kazemian, A., et al., Cementitious materials for construction-scale 3D printing: Laboratory testing of fresh printing mixture. Construction and Building Materials, 2017. 145: p. 639-647. https://doi.org/10.1016/j.conbuildmat.2017.04.015
7. Panda, B., et al., Current Challenges And Future Perspectives Of 3d Concrete Printing. 2018.

https://doi.org/10.1002/mawe.201700279

8. Jurrens Kevin, K., Standards for the rapid prototyping industry. Rapid Prototyping Journal, 1999. 5(4): p. 169-178. https://doi.org/10.1108/13552549910295514

9. Colla, V., et al., Large scale 3D printing: From deep sea to the moon. Low-Cost 3D Printing, for Science, Education & Sustainable Development; Canessa, E., Fonda, C., Zennaro, M., Eds, 2013: p. 127-132. http://citeseerx.ist.psu.edu/viewdoc/download?doi=10.1.1.410.790&rep=rep1&type=pdf#page=129

10. Dini, E., D-shape. Monolite UK Ltd. https://d-shape.com/, 2009.

11. Feng, P., X. Meng, and H. Zhang, Mechanical behavior of FRP sheets reinforced 3D elements printed with cementitious materials. Composite Structures, 2015. 134: p. 331-342. https://doi.org/10.1016/j.compstruct.2015.08.079

12. Lin, X., et al., Preparation and Application of 3D Printing Materials in Construction, in 27th Biennial Conference of the Concrete Institute of Australia. 2015: Melbourne, Australia

13. Lowke, D., et al., Particle-bed 3D printing in concrete construction – Possibilities and challenges. Cement and Concrete Research, 2018. 112: p. 50-65. https://doi.org/10.1016/j.cemconres.2018.05.018

14. Lee, C.S., et al., Measurement of anisotropic compressive strength of rapid prototyping parts. Journal of Materials Processing Technology, 2007. 187–188: p. 627-630. https://doi.org/10.1016/j.jmatprotec.2006.11.095

15. Khoshnevis, B., et al., Experimental investigation of contour crafting using ceramics materials. Rapid Prototyping Journal, 2001. 7(1): p. 32-42. https://doi.org/10.1108/13552540110365144

16. Lowke, D., et al., Particle bed 3D printing by selective cement activation – Applications, material and process technology. Cement and Concrete Research, 2020. 134: p. 106077. https://doi.org/10.1016/j.cemconres.2020.106077

17. Mechtcherine, V. and V.N. Nerella, 3D Printing with concrete: State-of-the art, trends, challenges. Bautechnik, 2018. 95(4): p. 275-287. https://doi.org/10.1016/j.conbuildmat.2018.05.202

18. Shakor, P., et al., Mechanical Properties of Cement-Based Materials and Effect of Elevated Temperature on Three-Dimensional (3-D) Printed Mortar Specimens in Inkjet 3-D Printing. ACI Materials Journal, 2019. 116(2): p. 55-67.

https://doi.org/10.14359/51714452

19. Shakor, P., et al., A Novel Methodology of Powder-based Cementitious Materials in 3D Inkjet Printing for Construction Applications in Sixth International Conference on the Durability of Concrete Structures. 2018, Whittles Publishing: Leeds, UK. https://docs.lib.purdue.edu/icdcs/2018/mid/7/

20. Mandal, S., et al., 3D powder printed tetracalcium phosphate scaffold with phytic acid binder: fabrication, microstructure and in situ X-Ray tomography analysis of compressive failure. Journal of Materials Science: Materials in Medicine, 2018. 29(3): p. 29. https://doi.org/10.1007/s10856-018-6034-8

21. Nemati, K.M., P.J. Monteiro, and N.G. Cook, A new method for studying stress-induced microcracks in concrete. Journal of materials in civil engineering, 1998. 10(3): p. 128-134. https://doi.org/10.1061/(ASCE)0899-1561(1998)10:3(128)

22. Shakor, P., et al., Review of Emerging Additive Manufacturing Technologies in 3D Printing of Cementitious Materials in the Construction Industry. Frontiers in Built Environment, 2019. 4(85). https://doi.org/10.3389/fbuil.2018.00085

23. Thomas, R.J. and S. Peethamparan, Effect of Specimen Size and Curing Condition on the Compressive Strength of Alkali-Activated Concrete. Transportation Research Record, 2017. 2629(1): p. 9-14. https://doi.org/10.3141/2629-02

24. ACI318-14, Building Code Requirements for Structural Concrete 2014: USA. https://www.concrete.org/store/productdetail.aspx?ItemID=318U14&Language=English

25. ASTM:C109/C109M, Compressive Strength of Hydraulic Cement Mortars (Using 2-in. or [50-mm] Cube Specimens). 2016. DOI: 10.1520/C0109_C0109M-20B

26. Systémes, D., Abaqus theory guide. Abaqus 6.13 Documentation, 2013. http://130.149.89.49:2080/v6.13/pdf_books/CAE.pdf

27. AS3700-2001, Masonry Structures. 2001. https://infostore.saiglobal.com/en-us/standards/as-3700-2001-99150_saig_as_as_257754/

28. Shakor, P., S. Nejadi, and G. Paul, Investigation into the effect of delays between printed layers on the mechanical strength of inkjet 3DP mortar. Manufacturing Letters, 2020. 23: p. 19-22. https://doi.org/10.1016/j.mfglet.2019.11.004

29. Barile, C., C. Casavola, and A. Cazzato, Acoustic emissions in 3D printed parts under mode I delamination test. Materials, 2018. 11(9): p. 1760. https://doi.org/10.3390/ma11091760

30. Farzadi, A., et al., Effect of layer thickness and printing orientation on mechanical properties and dimensional accuracy of 3D printed porous samples for bone tissue engineering. PLoS One, 2014. 9(9): p. e108252. https://doi.org/10.1371/journal.pone.0108252

31. Vaezi, M. and C. Chua, Effects of layer thickness and binder saturation level parameters on 3D printing process. The International Journal of Advanced Manufacturing Technology, 2011. 53(1-4): p. 275-284. https://doi.org/10.1007/s00170-010-2821-1

32. Zhou, Z., et al., Printability of calcium phosphate: calcium sulfate powders for the application of tissue engineered bone scaffolds using the 3D printing technique. Mater Sci Eng C Mater Biol Appl, 2014. 38: p. 1-10. DOI: 10.1016/j.msec.2014.01.027

33. Dini, E., D-shape Report. 2016. https://doi.org/10.2112/SI75-171.1